

Please cite the Published Version

Yan, B, Luo, M and Bai, Wei  (2019) An experimental and numerical study of plunging wave impact on a box-shape structure. *Marine Structures*, 66. pp. 272-287. ISSN 0951-8339

DOI: <https://doi.org/10.1016/j.marstruc.2019.05.003>

Publisher: Elsevier

Version: Accepted Version

Downloaded from: <https://e-space.mmu.ac.uk/622878/>

Usage rights:  [Creative Commons: Attribution-Noncommercial-No Derivative Works 4.0](https://creativecommons.org/licenses/by-nc-nd/4.0/)

Additional Information: This is an Author Accepted Manuscript of a paper accepted for publication by Elsevier in *Marine Structures*.

Enquiries:

If you have questions about this document, contact openresearch@mmu.ac.uk. Please include the URL of the record in e-space. If you believe that your, or a third party's rights have been compromised through this document please see our Take Down policy (available from <https://www.mmu.ac.uk/library/using-the-library/policies-and-guidelines>)

An experimental and numerical study of plunging wave impact on a box-shape structure

Bin Yan^a, Min Luo^{b,*}, Wei Bai^c

^aCollege of Civil Engineering, Shenzhen University, 3688 Nanhai Road, Nanshan District, Shenzhen 518060, China

^bCollege of Engineering, Swansea University Bay Campus, Swansea, SA1 8EN, UK

^cSchool of Computing, Mathematics and Digital Technology, Manchester Metropolitan University, Chester Street, Manchester M1 5GD, UK

Abstract

The plunging wave impacts on a box-shape structure are investigated experimentally and numerically, focusing on three typical scenarios with distinct features, i.e. the wave impact occurs after, upon and before wave breaking. In the experiments, the plunging wave is generated by a piston-type wave maker whose motion is governed by the focused wave theory. The fixed box-shape structure mimics the offshore platform structures. Measured are the wave elevations at typical positions, the wave impact pressures on the front and bottom (violent impact is very likely to occur) of the platform, and the wave profiles of the transient wave impact process. The experiment identifies the pressure maximums both on the front and bottom walls under three different wave impacts. The pressure oscillation along the front wall is observed and analyzed by examining the evolution of air cavity. The experimental parameters and dimensions including the actual wave maker motion signal was inputted into the numerical model to reproduce the same case. Numerical simulations using an improved immersed boundary method are compared with the experimental results with roughly good agreements being achieved. Besides, numerical pressure distributions along the front and bottom walls are presented to find different modes of wave impact. Finally, the maximal pressures on the front wall of the box-shape structure are normalized by two approaches, and compared with the documented maximal pressure ranges.

Keywords: Plunging wave, Pressure oscillation, Wave impact, Box-shape structure, Immersed boundary method

1. Introduction

As the global environment changes, extreme wave events may occur more frequently. With huge destructive power, those extreme waves can cause catastrophic damages to the offshore and coastal structures. The extreme wave impact process is quite complicated and still a challenging topic in the CFD (Computational Fluid Dynamics) community. In some circumstances, the extreme wave entraps some air, which seems to

*Corresponding author

Email address: min.luo@swansea.ac.uk (Min Luo)

6 significantly affect the local wave impact characteristics (Chan, 1994, Wood Deborah et al., 2000, Bredmose
7 et al., 2010). The highly non-linear water-air interaction makes this problem more complicated.

8 Extensive researchers have devoted their efforts to investigating the characteristics of wave impact. Black-
9 more and Hewson (1984) measured the impact pressure on Ilfracombe seawall in the field under broken waves
10 and found that the pressure was lower than those measured in the scaled experiments. The phenomenon
11 is ascribed to the high-percentage of air cavity. To account for the air volume fraction during an air en-
12 trapment process well, Blackmore and Hewson (1984) introduced a factor λ in the prediction of pressure p
13 under broken waves with an expression: $p = \lambda\rho C^2T$, where ρ , C and T are the water density, wave celerity
14 and wave period respectively. As the experiment cannot scale the high percentage of air entrained in the
15 wave by the Froude scaling law, it captured the relatively higher pressure value than the field observation.
16 Thus, the factor in the model test (1~10) is generally larger λ than that in the field observation (0.1~0.5).
17 The larger λ means more percentage of air is entrained in the wave, which can cause higher pressure. Chan
18 (1994) examined the pressure on a vertical wall subjected to the plunging wave impact. They concluded that
19 the impact pressure consists of two components: one related to normal wave evolution and the other one
20 determined by the air trapped. In the simulation of plunging wave on a vertical wall in Wood Deborah et al.
21 (2000), the presence of air did not prolong the peak pressure, but enlarged the magnitude of its impulse on
22 the structure.

23 Bullock et al. (2007) studied the wave impact on vertical and sloping walls experimentally, and found
24 that the characteristics of wave impact are highly dependent on the breaking condition. Particularly, this
25 study classified four different types of wave impact, i.e. slightly-breaking, low aeration, high-aeration and
26 broken wave impact. Considering one type of wave impact, in Bredmose et al. (2010), the experimental and
27 numerical simulations (the potential flow theory) for a flip-through wave impact on a typical seawall were
28 conducted. The results indicated that the impact pressure is extremely sensitive to the shape of impact
29 wave. Cuomo et al. (2010) conducted an experimental study on a vertical wall connected by a slope, who
30 normalized the pressure by $\rho g H_D$ (g is the acceleration of gravity and H_D is the designed wave height). The
31 experimental maximal normalized parameter of $\rho g H_D$ was almost 4.5. Bredmose et al. (2015) continued to
32 investigate the breaking impact on a typical wall and examined the effect of aeration. It found that more
33 aeration reduces the impact pressure and force on the wall.

34 For a simplification of a front wall of an FPSO (Floating Production Storage and Offloading) hull,
35 modeling a unidirectional breaking wave impacting a rigid wall was conducted in Guilcher et al. (2013) by
36 the SPH (Smoothed Particle Hydrodynamics) method. The results of two different scales were compared
37 with each other. The experiment at the scale 1:6 showed a higher pressure maximum in the aeration area
38 than that at the scale 1:1. This conclusion was also applied to the frequency of pressure oscillations. Smaller
39 scale experiment captured higher pressure value, which agreed with the conclusion in Blackmore and Hewson
40 (1984). With a Consistent Particle Method (CPM), Luo et al. (2016) simulated the dam break in a tank. The
41 pressures on the vertical boundary wall of the tank were recorded, indicating that the pressure oscillation is

42 closely linked with the compression or expansion of air pocket. For a better understanding of mechanics of
43 breaking wave impact, Hu et al. (2017) modeled four types of wave impact (slightly-breaking, flip-through,
44 large air pocket and broken wave impact) on a truncated wall in the numerical and experimental flumes.
45 Among four types of wave impact, the flip-through impact captured the highest pressure value.

46 In addition to the impact on the vertical wall, there are some papers focusing on the bottom of a structure.
47 Ren et al. (2006) investigated the flow field underneath a thin plate and impact pressure on the bottom wall.
48 The correlation between the impact pressure and water velocity was examined. Gao et al. (2012) studied the
49 regular wave impact on the bottom of a thin plate with an improved SPH method. The velocity and pressure
50 field near the structure were investigated. The pressure field along the bottom surface remained stable under
51 the regular wave condition. Abdussamie et al. (2016) adopted a thick deck (simplification of a tension leg
52 platform) to study the wave impact, but they only focused on the impact event over the bottom wall. The
53 static set-down of the deck had a significant effect on the loads over the bottom surface of deck. Qin et al.
54 (2017) carried out a numerical simulation of nonlinear freak wave impact underneath a fixed horizontal 2D
55 deck. It observed that under the freak wave conditions, large wave impact may happen with a relatively big
56 deck clearance (e.g. the survival draft of deep-sea platforms). It also found a strong effect of deck clearance
57 on the loads over the bottom wall of deck.

58 Most of the above-mentioned studies investigated the wave impacts on a vertical wall or on the bottom
59 surface of thin plate structures. For the box-shape structures such as the oil/gas platform, the wave impacts
60 on both the top and bottom of the structure are critical factors, which should be comprehensively considered
61 in the design. In this context, this study investigates the typical extreme wave impacts on the bottom and
62 front wall of a fixed box-shape structure, through carefully controlled experiments and numerical simulations,
63 which has been rarely investigated before. The characteristics of the wave impact pressure under different
64 wave impact scenarios with quite small time intervals are focused. More importantly, the oscillation of wave
65 impact pressure on the front wall of the structure is observed and its correlation with the air entrapment
66 is explored, which is so far not well understood. The experimental elevations and pressures are employed
67 to validate the numerical method (immersed boundary method, Yan et al. (2018)). Using the validated
68 numerical method, the impact pressure distributions on the front and bottom walls of the structure are
69 investigated. The peak pressure values are analyzed and found to be located within the range documented
70 by Blackmore and Hewson (1984) and Cuomo et al. (2010).

71 **2. Experimental investigation**

72 *2.1. Experimental setup*

73 An experimental study is conducted in the ferrocement wave flume ($36\text{ m} \times 2\text{ m} \times 1.3\text{ m}$) in the hydraulic
74 laboratory at National University of Singapore. Waves are generated by a piston type wave paddle. The
75 downstream end of the wave flume is a sloping beach that absorbs wave and hence minimizes the wave
76 reflection. The platform structure is a hollow box of 0.12 m height and of 0.5 m length (along the wave

77 flume direction), made of perspex of 10 mm thickness. The platform is of width 1.95 m and installed in the
78 middle of the wave flume. Hence there is a 2.5 cm gap at each side of the platform from the flume wall (for
79 ease of structure installation). The ratio of the gap distance to the flume width is 1.25 %. Such a small gap
80 has a limited influence on the wave motion. In addition, the influences exist mainly near the flume wall.
81 Therefore, the wave motion near the flume center can be reasonably assumed to be two-dimensional (2D).
82 Considering that all the measurements of wave elevations and pressures are on the center line of the wave
83 flume, the gaps at both sides and the water entered do not produce significant nonlinear forces that differ
84 from a perfect 2D case. Stiffeners are added in the platform to stiffen the walls of the platform, ensuring
85 that the platform performs as a rigid body. The platform is fixed by a vertical support plate, which is
86 supported by a steel frame from the downstream side. The maximum lateral deflection of the platform
87 was around 2 mm, being very small compared to the structure dimension. In addition, the frequency of
88 the structural lateral deflection (around 1 Hz) is more than one order of magnitude away from those of the
89 pressure responses on the platform (the values can be seen from Figs. 5 and 7). Therefore, the effect of the
90 tiny structural deflection on the pressure and force responses on the structure is negligible. The bottom of
91 the platform is 0.749 m from the flume bottom, 0.049 m above the mean water level. The front wall of the
92 platform is 13.771 m from the initial position of the wave paddle (see Fig. 1(a)). Four ATM.1ST analogy
93 gauge pressure sensors of measurement range 0.1 bar (accuracy is 0.1 % full scale and response time is less
94 than 1 millisecond) are installed on the upstream part of the platform to measure the extreme wave impact
95 pressures at typical positions. Their positions are shown in Fig. 1(b) and Fig. 1(d): FP1 and FP2 at the
96 front, and BP1 and BP2 at the bottom. To measure the wave elevations, three wave gauges are installed at
97 6.694 m, 9.459 m and 10.904 m respectively from the wave paddle on the center line of the wave flume. A
98 high-speed camera is placed perpendicular to the glass wall of the wave flume, near the platform, to capture
99 the transient wave motion.

100 2.2. *Plunging wave generation*

101 The plunging wave is generated using the focused wave theory. The basic idea is that a group of linear
102 waves with different frequencies propagate at different velocities and their crests occur simultaneously at
103 a specified point in space and time, producing a large amplitude wave, which will develop into a plunging
104 breaker subsequently. By superposition of all wave components, the wave elevations with space x and time
105 t is as follows (Ma et al., 2009; Zhao and Hu, 2012),

$$\eta(x, t) = \sum_{i=1}^N a_i \cos [k_i(x_i - x_f) - 2\pi f_i(t - t_f)]. \quad (1)$$

106 The meanings of those variables in Eq. 1 are presented in Table 1. The theoretical amplitude of the focused
107 wave at the focusing position is the summation of a_i (0.197 m for the three wave cases), but the actual
108 wave amplitude is smaller than this value because of wave nonlinearity. Three wave impact scenarios are
109 studied, i.e. wave impacts on the platform before, upon and after wave breaking, by changing x_f in Eq. 1

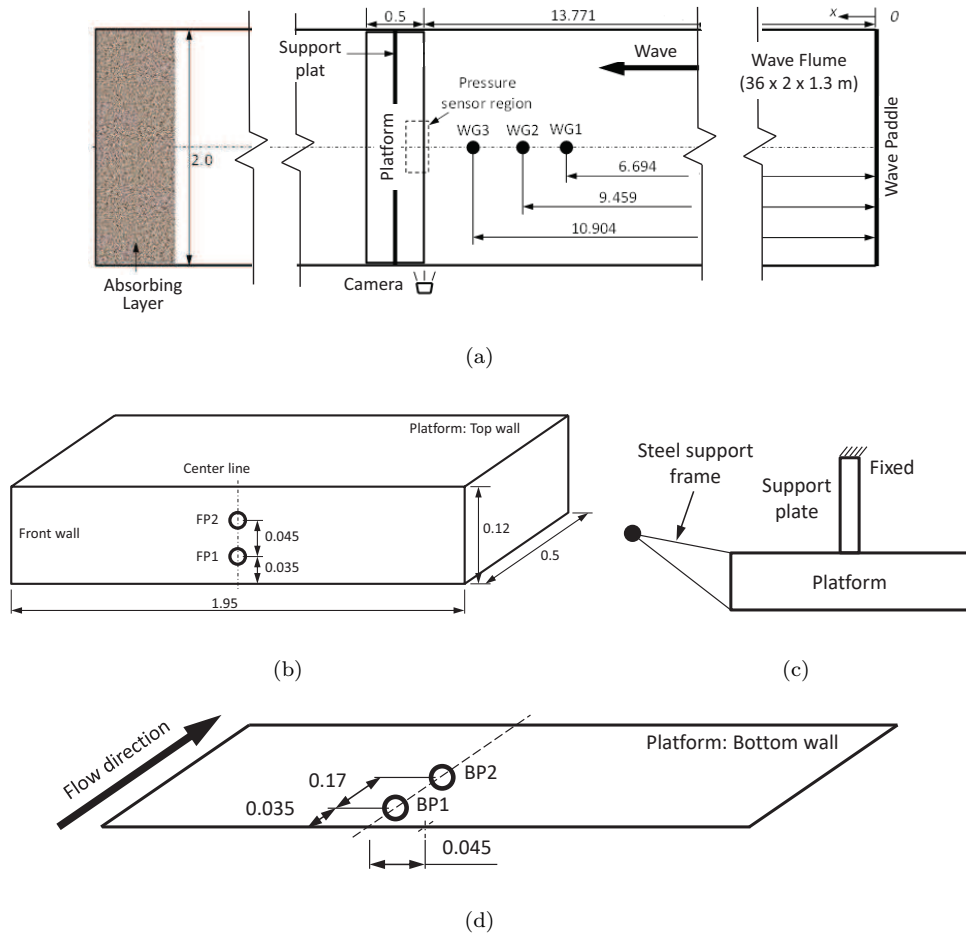


Figure 1: Schematic view and dimension of the experimental setup (unit: m): (a) plan view; (b) platform and sensor hole positions; (c) section view of the platform; (d) bottom wall of the platform.

Table 1: Plunging wave parameters

Water depth	d	0.7m
Number of wave components	N	32
Frequency band	$[f_{min}, f_{max}]$	[0.32Hz, 0.96Hz]
Amplitude of the i -th component	a_i	0.0061m (Chan, 1994)
Frequency of the i -th component	f_i	Uniformly selected in the frequency band
Wave number of the i -th component	k_i	Computed by dispersion equation
Characteristics wave frequency	$f = (f_{min} + f_{max})/2$	0.64Hz
Characteristics wave length	L	3.312m
Characteristics wave celerity	C	2.11m/s
Focusing position / time	x_f / t_f	12.4m / 20.832s (Impact after breaking, S1) 12.45m / 20.857s (Impact upon breaking, S2) 12.8m / 20.902s (Impact before breaking, S3)

110 (and hence the wave breaking location) so as to investigate the characteristics of wave impact on a structure
 111 with the wave forms before the impact occurs. Once the target wave is specified, a transfer function (Biesel
 112 and Suquet, 1951) is used to compute the wave paddle motion. The focusing time t_f is determined in such
 113 a way that the paddle motion is zero when $t = 0$. In the experiments, the actual wave paddle displacements
 114 are measured by a linear variable differential transformer (LVDT). As shown in Fig. 2, the measured paddle
 115 motion matches well with the theoretical paddle motion. It shows the precision of the paddle control system.
 116 Based on measured paddle motion, the wave paddle velocities are computed and used as the excitation input
 117 in the numerical simulations.

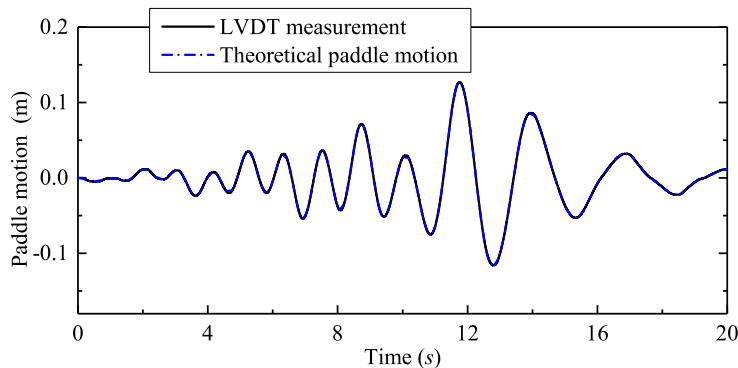


Figure 2: Wave paddle motion: control system input VS. LVDT of S2 measurement.

118 Three wave packets are generated and the associated parameters are presented in Table 1. Those three
 119 wave packets have the same wave frequency and amplitude components. The difference between them is
 120 the focal position (and hence focal time). Particularly, in S1 the wave packet focuses at a nearest position

121 from the wave paddle. Wave packets S2 and S3 focus at a middle and furthest position, respectively. The
 122 focal positions of three cases are designed such that the wave breaks already (S1), just breaks (S2) and
 123 does not break yet (S3) in the wave interaction with the structure. This allows an investigation on how the
 124 wave profile (upon wave impact occurs) affects the dynamic wave impact process, by keeping the same wave
 125 energy input (Hu et al., 2017).

126 *2.3. Experimental results*

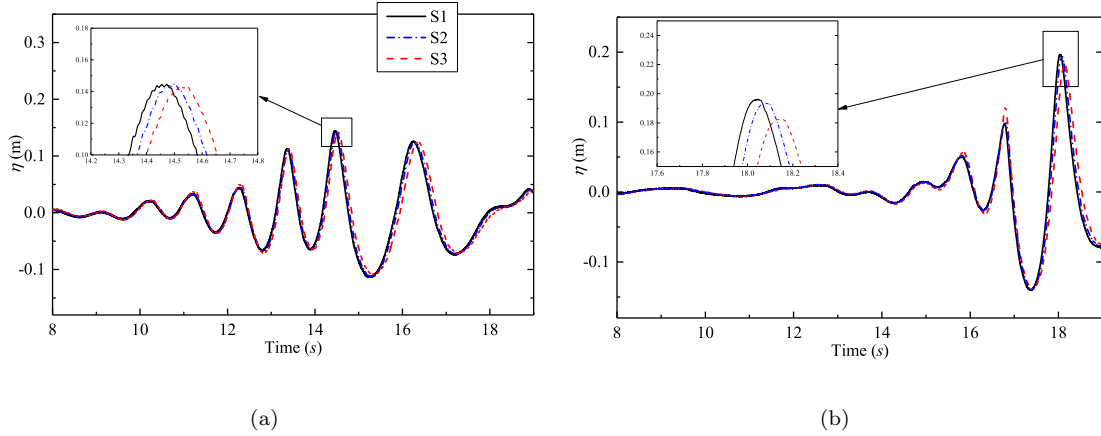


Figure 3: Experimental wave elevations with different inputted signals (S1, S2, S3): (a) WG1; (b) WG3.

127 As shown in Fig. 3, the time histories of wave elevation at WG1 and WG3 of three cases are presented.
 128 Due to the wave focusing, a large wave appears at WG3 with the amplitude of almost 0.197 m. The subtle
 129 difference between the three cases is the phase lag revealed in Table 1 and the magnitude of wave height. The
 130 waves of S1 and S2 possess a similar wave height while the wave of S3 has a smaller wave height compared
 131 to those of S1 and S2. The maximal wave height occurs in S1, shown in Fig. 3(b), is about 0.34 m, resulting
 132 in a very high wave steepness (about 0.1). The larger wave steepness easily leads to wave breaking.

133 Fig. 4 gives the snapshots of wave profile during the transiting period when the wave approaches and
 134 interacts with the platform. The wave of S2 breaks as soon as it impacts the deck, while the wave of S3
 135 is non-breaking when it reaches the front wall of the deck. For the wave of S1, it impacts the front wall of
 136 the deck after breaking. The waves of S1 and S2 show the breaking features, whereas the wave of S3 is still
 137 developing in front of the deck. In addition, the waves of S1 and S2 entrap more air than that of S3. The
 138 air entrapment has a significant influence on the impact pressure, which will be discussed later. Based on
 139 those features and the categorization from Hu et al. (2017), these three wave impacts can be classified as
 140 the corresponding types. The impacts of S1 and S2 correspond to large air pocket impact while the impact
 141 of S3 belongs to slightly-breaking impact.

142 Fig. 5 shows the time histories of pressure at four stations under three wave conditions. For the pressure
 143 at BP1, three waves lead to the similar magnitude of impact pressure about 4.0 kpa. More details about

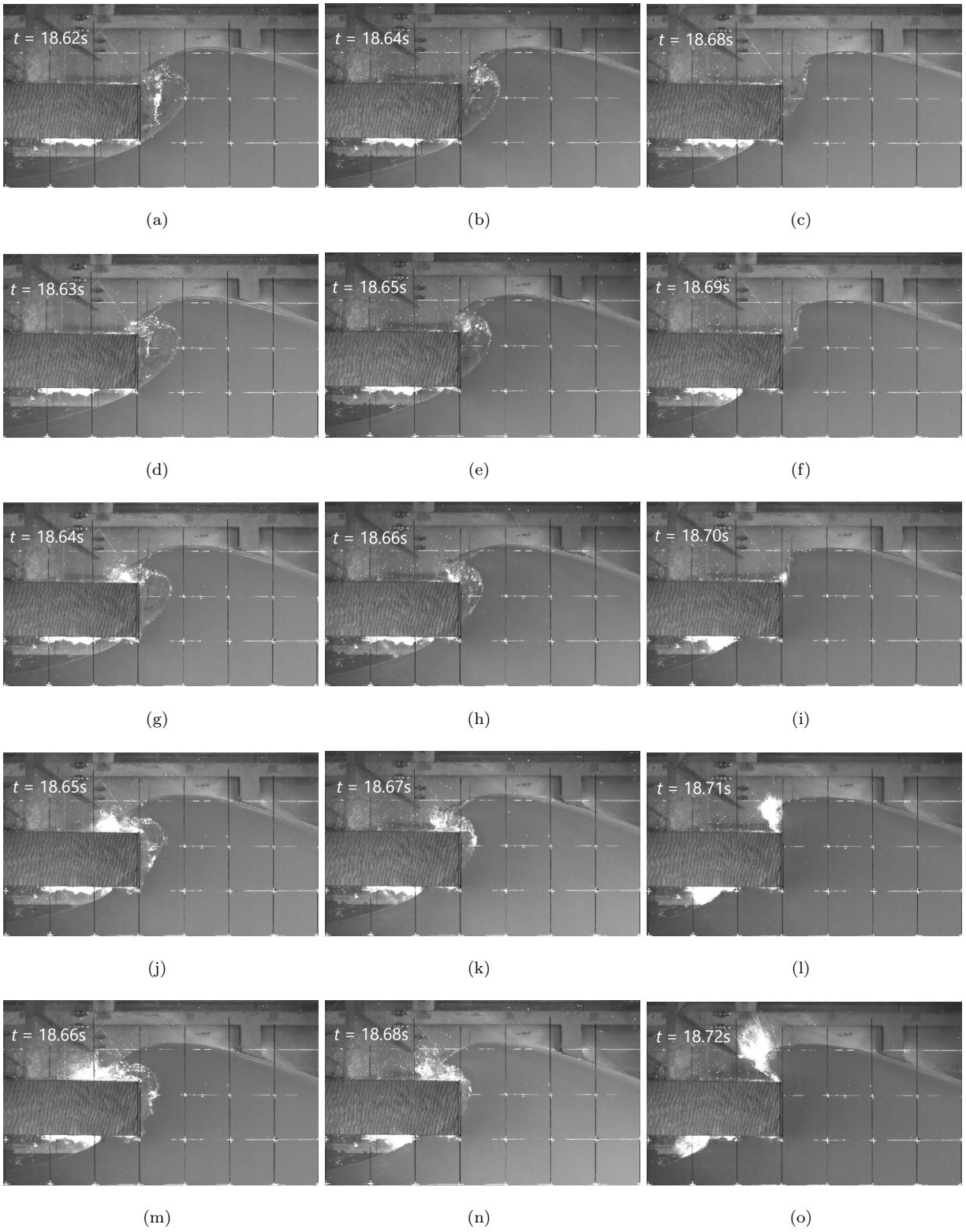


Figure 4: Snapshots of the wave impact process for the three wave scenarios. Left column: S1; middle column: S2; right column: S3.

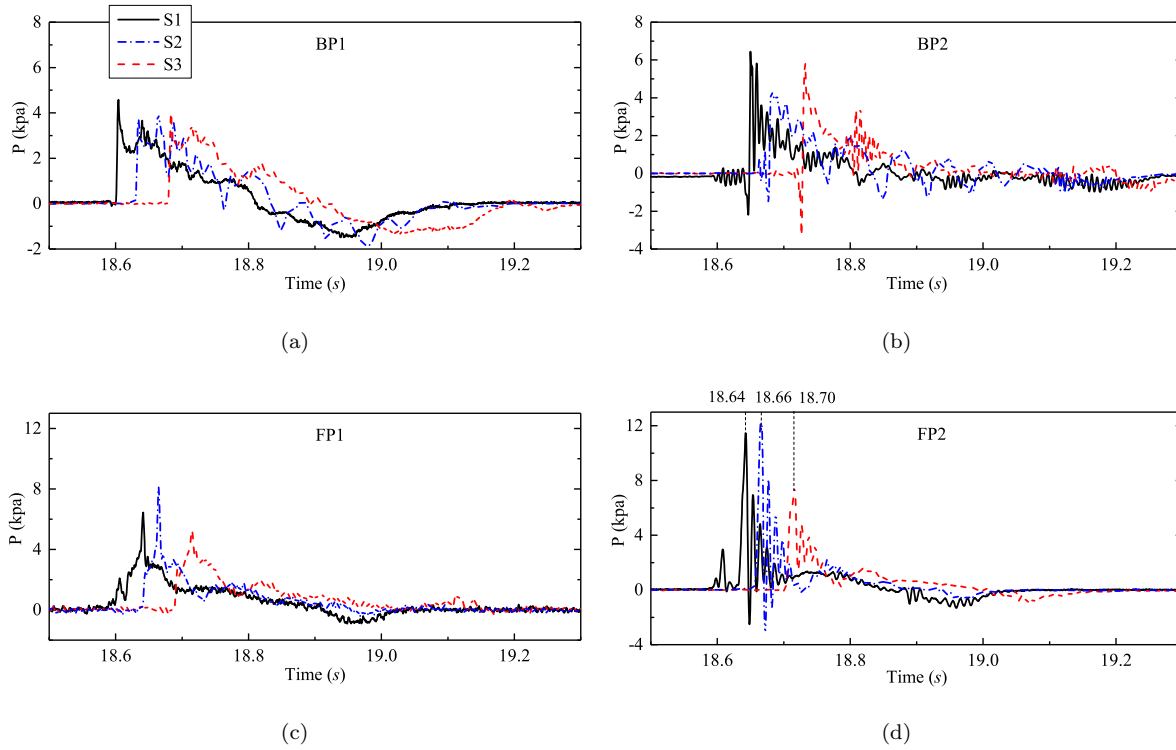


Figure 5: Comparison of pressure among three types of plunging waves (S1, S2, S3) at various positions: (a) BP1; (b) BP2; (c) FP1; (d) FP2.

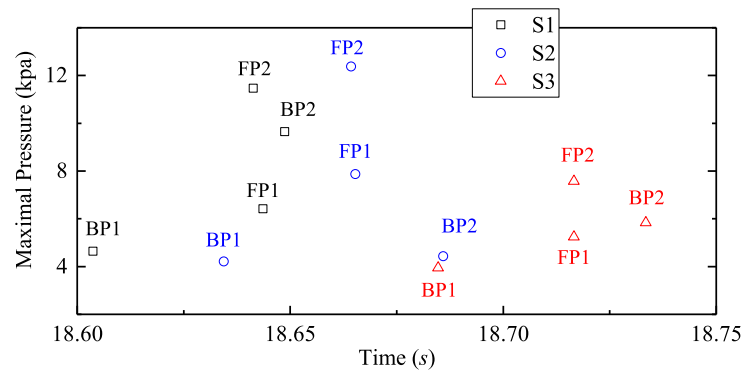


Figure 6: Occurrence of maximal pressure among three types of plunging waves.

Table 2: Maximal positive and negative pressures in the three cases.

Stations	Maximal positive pressure /kpa			Maximal negative pressure /kpa		
	S1	S2	S3	S1	S2	S3
BP1	4.648	3.946	3.846	-1.468	-1.836	-1.368
BP2	6.501	4.332	5.933	-2.178	-1.551	-3.067
FP1	6.475	8.184	5.126	-0.957	-0.399	-0.236
FP2	11.475	12.162	7.532	-2.493	-3.204	-1.015

144 the maximal positive and negative pressures are listed in Table 2. In addition to the impact pressure, this
 145 station is also subjected to suction pressure (negative), which is about 2.0 kpa in three situations. Secondly,
 146 Fig. 5(b) shows the pressure at another station on the bottom surface, which is farther downstream than
 147 BP1. As BP2 is closer to the water front underneath the deck in the wave propagation, the interaction
 148 between the wave front and bottom wall of deck is stronger. Thus, BP2 captures a larger peak pressure
 149 value than BP1. At BP2, the suction pressure approaches 3.0 kpa, but with the shorter time duration than
 150 that at BP1. In addition, an evident pressure oscillation around $t = 18.8$ s is observed when the wave impacts
 151 the bottom wall in S3. It may be caused by the entrained air around the bottom wall, which is easy to be
 152 formed in S3 (see Fig. 4(o)). The mechanism is similar to the pressure oscillation on the front wall of the
 153 platform (see the FP2 result in Fig. 5). The phenomenon was also pointed out by Faltinsen et al. (2004)
 154 and Lind et al. (2015).

155 The pressures on the front wall are presented in Fig. 5(c) and Fig. 5(d), where the higher maximal pressure
 156 values than those along the bottom surface are observed and approaching 12.0 kpa. The magnitude at FP1
 157 is slightly smaller than that at FP2. As the position of FP1 is lower than FP2, FP1 is easily submerged
 158 by the water in the wave impact process and affected less by the air cavity than FP2. Thus, the station
 159 FP1 captures a smaller peak pressure. Compared with Fig. 5(c), there exists the larger negative pressure in
 160 Fig. 5(d). Both the negative pressures at BP2 and FP2 are higher than those at BP1 and FP1. It may be
 161 caused by the more air entrained around the positions BP2 and FP2 (see Fig. 4), which easily leads to the
 162 pressure oscillation. The pressure oscillation may be induced by the escape or inflation of air cavity around
 163 the bottom and front walls. The phenomenon was also pointed out by Chan and Melville (1988) and Hu
 164 et al. (2017).

165 The peak pressures and their time instants of occurrence of the three cases are plotted in Fig. 6. In all
 166 three cases, the maximal pressure occurs at FP2. The maximal pressure at BP1 appears earlier than those
 167 at FP1 and FP2, while the pressure at BP2 approaches its maximum later than those at FP1 and FP2. The
 168 station FP1 contacts the water earliest and the wave impact on the front wall occurs successively after that
 169 at FP1. And BP2 is farther than BP1 and the front wall. Thus, the wave impact at BP2 occurs at last.

170 *2.4. Pressure Oscillation*

171 The last subsection shows the pressure oscillation observed at FP2 for the waves of S1 and S2. More
 172 details are reflected in Fig.7, where the pressure oscillation is zoomed in. The pressure time history reveals
 173 a stable oscillation period $T = 0.011$ s for both the waves of S1 and S2. Both Topliss et al. (1993) and
 174 Abrahamsen and Faltinsen (2012) derived the formula of the natural frequency for the air pocket on a
 175 vertical wall, in which the shape of air pocket was assumed to be a semi-circle. Abrahamsen and Faltinsen
 176 (2012) also claimed that the frequency is related to the shape of air cavity and water surface outside the air
 177 cavity. Lugni et al. (2010) threw a deep insight into the mechanism of the pressure oscillation.

178 According to Lugni et al. (2010), the pressure oscillation is divided into three regimes: The first peak
 179 (Regime A), the damped oscillation (Regime B), and small amplitude fluctuation (Regime C). Similarly, the
 180 pressure oscillation in the present experiment is categorized in three regimes: the first peak (Regime I, first
 181 period), the damped oscillation (Regime II, the subsequent four periods), and small amplitude fluctuation
 182 (Regime III, after five periods). In Regime I, the peak pressure is induced by the closure of the air cavity,
 183 which causes very large acceleration of water to the front wall. The second regime (Regime II) is the
 184 damped oscillation, in which the amplitude is strongly related to the wave front evolution. Thus, the air
 185 cavity evolution influences the pressure amplitude as the wave front evolution is affected by the air cavity
 186 evolution. In Fig. 7, the oscillation is not strictly damped that the trough shifts downward at the fourth
 187 period both for the waves of S1 and S2. For Fig. 7(a), the oscillation continues to be damped after the fourth
 188 period while the troughs of fourth and fifth period in Fig. 7(b) are still shifting downward. The remaining
 189 part (Regime III) governed by the gravity on the water volume along the front wall, resulting in very small
 190 amplitude fluctuation.

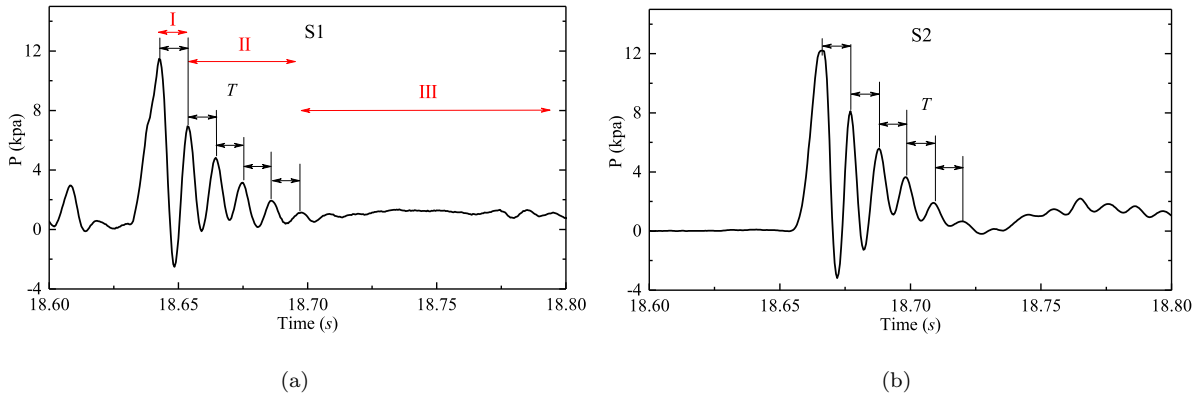


Figure 7: Detail of pressure oscillation at FP2 of the wave of S1 and S2: (a) S1; (b) S2.

191 To elucidate the mechanism of air cavity evolution, the snapshots of air cavity for five periods in Regime
 192 I and II are listed in Fig. 8. The shape of air cavity is marked by the red line. In S1, the air cavity appears
 193 around two corners of the front wall while the air cavity just surrounds the upper corner of the front wall

Table 3: Maximal pressure on the front wall..

S1	Area of air cavity (cm ²)	Amplitude (kpa)	S2	Area of air cavity	Amplitude (kpa)
1T	78	11.552	1T	72	12.259
2T	51	7.011	2T	49	8.089
3T	43	4.835	3T	40	5.568
3T	58	3.098	4T	43	3.687
3T	54	2.035	5T	51	1.946

194 for the S2 case. The area of air cavity of S1 is larger than that of S2. In the first three periods for both S1
 195 and S2 cases, the air cavity becomes smaller that the air escapes through the wave front. From the fourth
 196 period, the air cavity is inflated. Generally, the air inflation would result in the enlarged negative pressure
 197 value.

198 As indicated by Lugni et al. (2010), the pressure amplitude is highly dependent on the wave front
 199 evolution. It also means that the air cavity influences the pressure amplitudes because of the close relationship
 200 between the wave front evolution and air cavity. Thus, the area of air cavity is tracked to evaluate the pressure
 201 amplitudes. Orthogonal grids of uniform spacing are attached to the high-resolution images of wave snapshot
 202 to roughly estimate the area of air entrapment zone, as shown in Fig. 9. As the boundary (red line) of the
 203 air cavity is figured out, the area enclosed can be computed by counting the number of air cavity.

204 The area of air cavity and the amplitude of peak pressure for the cases of S1 and S2 are presented in
 205 Table 3. The amplitudes decrease monotonically while the area of air cavity decreases first and increases at
 206 last two periods. It is recalled that the phenomena in Fig. 7, Fig. 7(a) just shows one enlarged trough while
 207 Fig. 7(b) reveals two enlarged troughs. The reason may be the inflation of the air cavity, as indicated in
 208 Table 3. The air cavity of S1 becomes larger from 43 to 58 cm² and reduces to 54 cm². The air cavity of
 209 S2 continues to increase from 40 to 43 and 51. That is why S1 experienced one trough shifting downward
 210 while there are two troughs shifting downward in S2. If the value in Table 3 is normalized by maximal value
 211 in each column, the normalized scatter spots can be plotted in Fig. 10. In the first three periods, both the
 212 pressure amplitude and area of air cavity decrease. After the third period, the area of air cavity is inflating
 213 while the damped pressure amplitude is decreasing.

214 2.5. Repeatability test

215 Several studies have reported the variability of wave impact pressure in different repeats of the same case
 216 (Chan and Melville, 1988; Chan, 1994). The variations are mainly attributed to the experimental errors (e.g.
 217 real paddle motion and the initial condition of the fluid domain) and the randomness in the breaking-wave
 218 kinematics. To check the repeatability of the present experiment. S2 was repeated for three times. Before
 219 each test, the water in the wave flume is stationary so as to minimize the error from this factor. Because
 220 of those operations, the experimental errors in this repeat test are negligible. The pressure time histories of

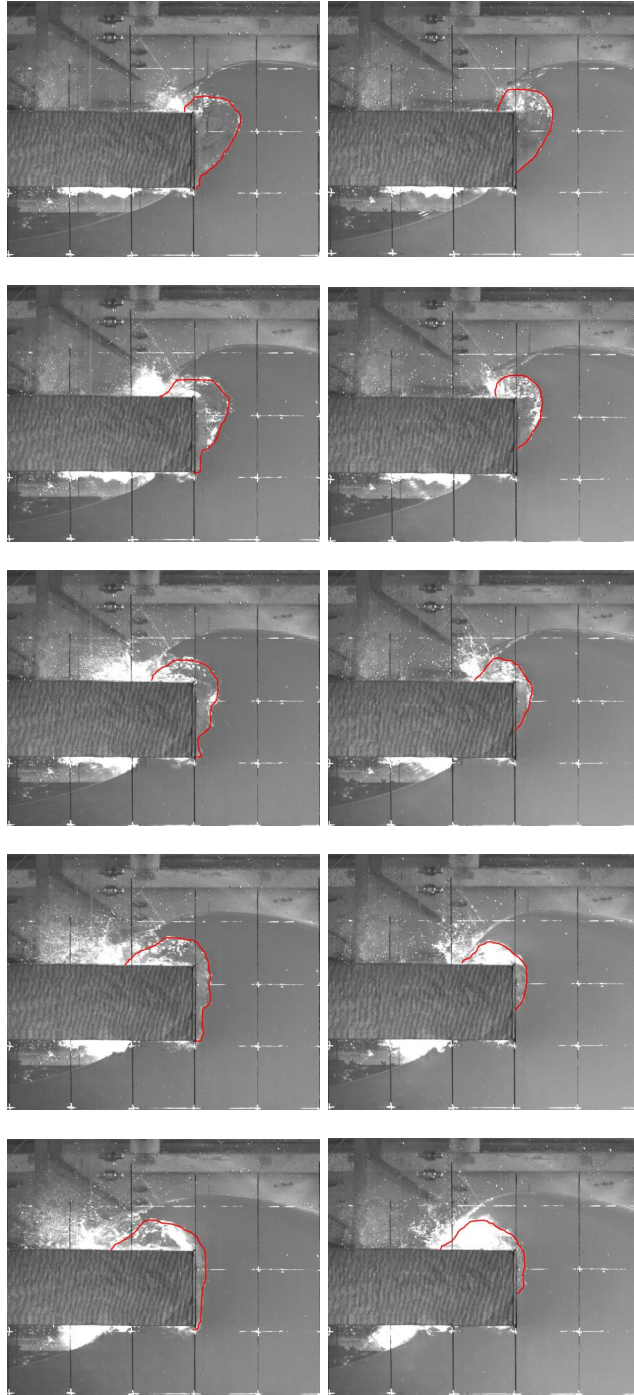


Figure 8: Snapshots of the air cavity evolution for two tests of S1 and S2. Left column: S1; Right Column: S2. The red solid line encloses the air cavity.

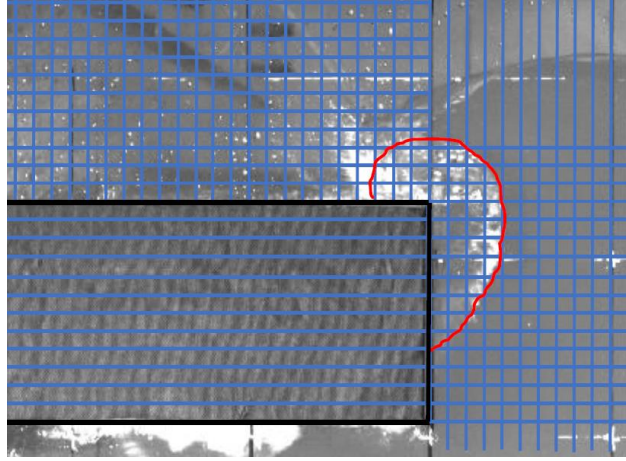


Figure 9: Sketch of the orthogonal grids attached to the wave snapshot to roughly estimate the area of air cavity. The solid black line stands for the shape of deck; The red line encloses the shape of air cavity.

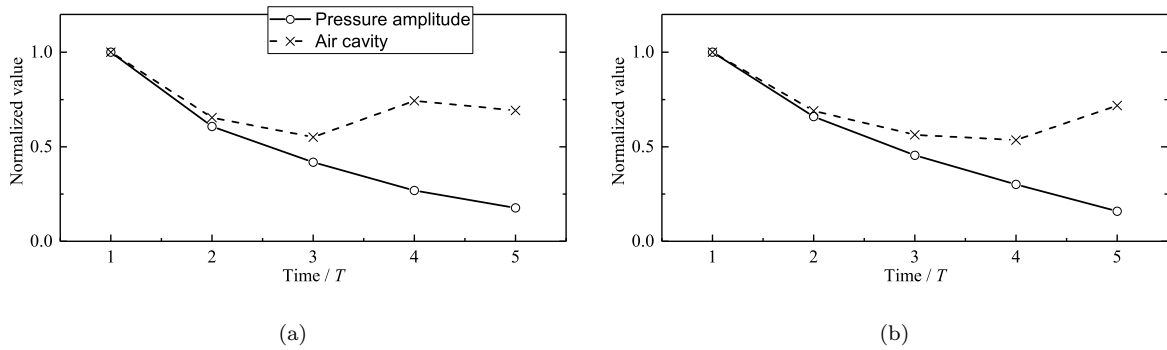


Figure 10: The relation between the pressure amplitude and area of air cavity.

221 three repeats are shown in Fig.11. The maximum variance in the whole time series is Fig.11(b), which is
 222 quite small. From Fig. 11, it can be seen that the pressure histories at the four measurement locations have
 223 almost the same general features and peak values although some minor differences exist. This is different
 224 from Chan and Melville (1988) and Chan (1994) who reported that the maximal pressure can vary by more
 225 than 100%. If the pressure variability does exist, one possible reason is that the measuring diaphragm (a
 226 circle of diameter 18mm) of the pressure sensor used in this study measures the average pressure of a finite
 227 area and hence the randomness in the extreme wave impact is filtered out. To reveal the detailed physics of
 228 this phenomenon, future researches are needed.

229 The repeatability can be further supported by the wave shape, as shown in Fig.12. The figure lists out
 230 the wave shapes for three tests when the wave is impacting the deck. The snapshots in each column present
 231 very similar wave shape, especially the wave front and the air entrained. In other words, the wave shape
 232 shows less variability for three repeating tests.

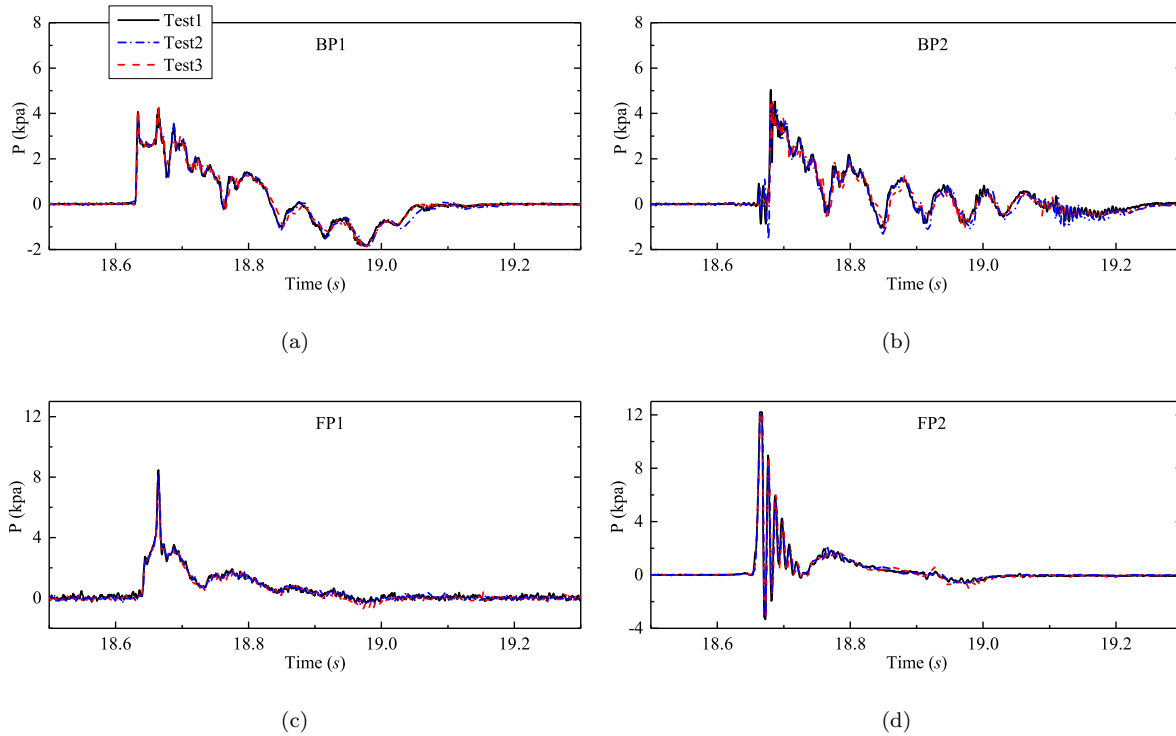


Figure 11: Repeatability test of pressure evolution at four gauges under the signal S2. Three test are presented.

233 3. Numerical simulation

234 In the numerical simulation, a Navier-Stokers solver combining with a level set method (Archer and
 235 Bai, 2015) is adopted to simulate the two-phase flow. The structure is modeled by an improved immersed
 236 boundary method from Yan et al. (2018). The detail is as follows.

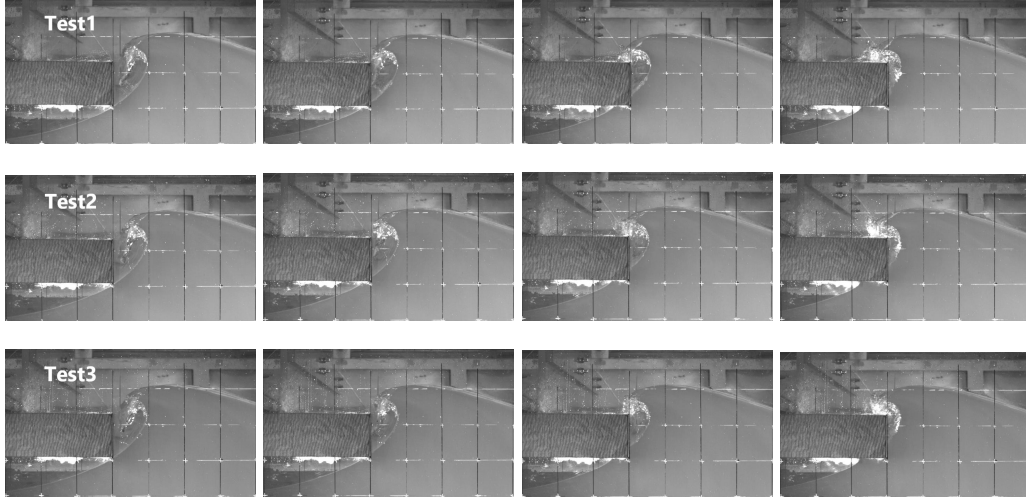


Figure 12: Snapshots of the wave impact process for three tests of S2. First row: Test1; middle row: Test2; third row: Test3.

237 3.1. Two-phase flow solver

238 For the 2D incompressible viscous fluid motion, the Navier-Stokes equations are used as the governing
 239 equations, including the momentum equations,

$$\frac{\partial u_i}{\partial t} + u_j \frac{\partial u_i}{\partial x_j} = \frac{1}{\rho} \left(-\frac{\partial p}{\partial x_i} + \frac{\partial \tau_{ij}}{\partial x_j} \right) + g_i + f_i, \quad (2)$$

240 and the continuity equation,

$$\frac{\partial u_i}{\partial x_i} = 0, \quad (3)$$

241 where u_i is the fluid motion velocity, located at the cell center face in a staggered grid system, x_i the orthog-
 242 onal coordinate in space, t the time. For the variables at the cell center, p is the pressure, g_i the acceleration
 243 of gravity, ρ the fluid density, τ_{ij} the viscous stress components with the use of the Cartesian notation.
 244 Besides, f_i is the momentum added around an immersed boundary interface to model the structures.

245 A finite difference method is utilized to discretize the Navier-Stokes equations. The above variables are
 246 updated by a fractional step method (Archer and Bai, 2015). More details about discretizations are shown
 247 in Archer and Bai (2015) and Yan et al. (2018).

248 To capture the complicated wave surface, the level set method is adopted with the definition of a scalar
 249 distance function ϕ , which is to measure the shortest distance from the grid cell center to the interface. The
 250 distance function ϕ satisfies a convective equation,

$$\frac{\partial \phi}{\partial t} + u_i \frac{\partial \phi}{\partial x_i} = 0. \quad (4)$$

251 In the convective equation, the term $\frac{\partial \phi}{\partial x_i}$ is treated numerically by the fifth-order HJ-WENO scheme
 252 (Jiang and Peng, 2000). To continue, the value of ϕ at the next time-step can be updated by a third-order
 253 RK-TVD scheme, as indicated by Archer and Bai (2015).

254 3.2. Immersed boundary treatment

255 For the fluid-structure interaction, the solid phase is realized by adding a momentum forcing term near
 256 the boundary. The position of velocity vector that adds the forcing momentum term is defined as the forcing
 257 point. As the velocity vector is based on the staggered grid system, the boundary can not always coincide
 258 with the forcing points. Thus, the momentum forcing term should be calculated at the forcing points rather
 259 than enforced directly. Firstly, the forcing points ought to be located. To present a brief procedure for the
 260 forcing point search, Fig. 13 shows a sketch for illustration. In the figure, the line segment x_1 - x_2 indicates
 261 the boundary and the solid phase is represented by the shadowed area. The procedure for locating forcing
 262 points can be seen in Yan et al. (2018), where the clear details were given.

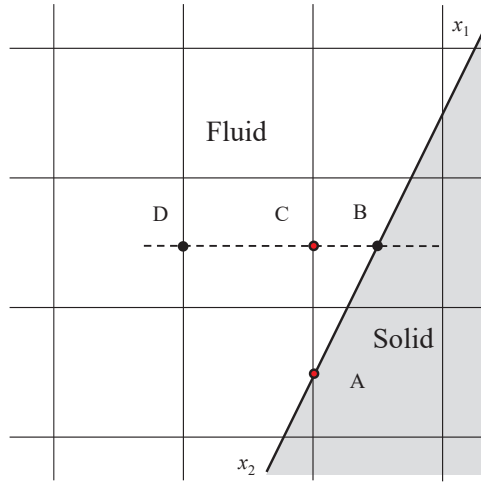


Figure 13: Illustration of the location and determination of imposed forcing component.

263 Since the forcing point is known, the predicted forcing component at the forcing point is based on the
 264 formula described in Mohd-Yusof (1997). The forcing term can be simply predicted by the following formula,

$$f_i = \frac{u_f - u_i^{n-1}}{\Delta t} - RHS_i^{n-1}. \quad (5)$$

265 where RHS is a sum of the convective, viscous, pressure gradient and body force terms in Eq. 2, the
 266 superscript $n-1$ denotes the value at the previous time step, and u_f is the velocity at the forcing point.
 267 If the forcing point is on the solid boundary, such as Point A in Fig. 13, $u_f = u_A$. Otherwise, u_f has to
 268 be calculated via the interpolation procedure from the surrounding flow field. Thus, the value of u_f can
 269 be interpolated via the velocities at Points B and D. Finally, the enforced momentum forcing term f_i is
 270 obtained.

271 *3.3. Comparison of experimental and numerical results*

272 The numerical model is validated against the experimental data. In the numerical simulations, in the
273 region between the wave maker and the rear of the platform, the uniform mesh sizes along the horizontal
274 and vertical directions are chosen to be 0.01 m and 0.005 m, respectively. In the rest area, the grid intervals
275 of 0.02 m and 0.01 m in the horizontal and vertical directions are adopted. These grids ensure that the wave
276 free surface can be captured and the structure can be modeled with good accuracy. For all three cases, the
277 simulation of process of 20 s takes about 24 hours on a desktop PC with the CPU of Intel(R) Core i7-6700.
278 As shown in Fig. 14, the wave elevations at WG1 and WG3 predicted by the present numerical model are in
279 generally good agreement with the experimental measurements except that the wave crests and troughs are
280 slightly underestimated with the difference about 4.1% and 2.8% at WG1 and WG3 respectively. Such small
281 difference is probably due to the error of input signal. In the numerical simulation, the wave is generated by
282 the velocity signal of wave paddle, while the experiment provides the displacement signal of wave paddle. The
283 transformation from the displacement signal to velocity signal is carried out by the numerical differentiation
284 over time where the error may occur. From the cases of S1 and S2, a minor difference between inputted
285 signals could lead to the significant difference in wave elevations and pressures, as indicated in Figs. 4 and 5.

286 Fig. 15 shows the comparison of pressure time history between the experimental and numerical data. The
287 trend of experimental pressure is captured well by the numerical model and the pressure magnitude at all
288 four stations are underestimated. For the pressure at FP2, the impulse value is captured better than those
289 at other three stations. Although the differences between the numerical and experimental wave elevations
290 are generally small in Fig. 14, they may continue to grow just in front of the platform, which will cause a
291 relatively larger discrepancy in wave impact pressures. In addition, the resolution of measurement equipment
292 for wave elevation and pressure is also different. Finer mesh sizes have been tried, but the numerical results
293 are very similar to the present ones. The pressure oscillation in the experiment is not reproduced (see
294 Fig. 15(j) and Fig. 15(k)), because the air compressibility is not considered in the numerical model. In
295 general, the developed numerical model is able to capture the key features of the wave elevation and impact
296 pressure during a plunging wave impact process. Using the validated model, more detailed investigations on
297 the wave impact pressure on the platform are conducted, as elaborated in the following two subsections.

298 *3.4. Pressure distribution on the structure*

299 It is costly and sometimes practically impossible to do a fine-resolution measurement of the pressure
300 distribution on a structure. In contrast, such work can be done easily once a reliable numerical model is
301 developed. Based on the validated numerical model, the pressure distributions at typical time instants on
302 the front and bottom walls in the three cases are studied as shown in Fig. 16 and Fig. 17.

303 Firstly, the pressure distributions along the vertical front wall under the three wave scenarios are presented
304 in Fig. 16. Fig. 16(a) captures a peak value 10.21 kpa around $y = 0.832$ m on the front wall in S1, which is
305 close to the instant $t = 18.64$ s shown in the sub-figure of Fig. 4. The water jet licks the front wall with a

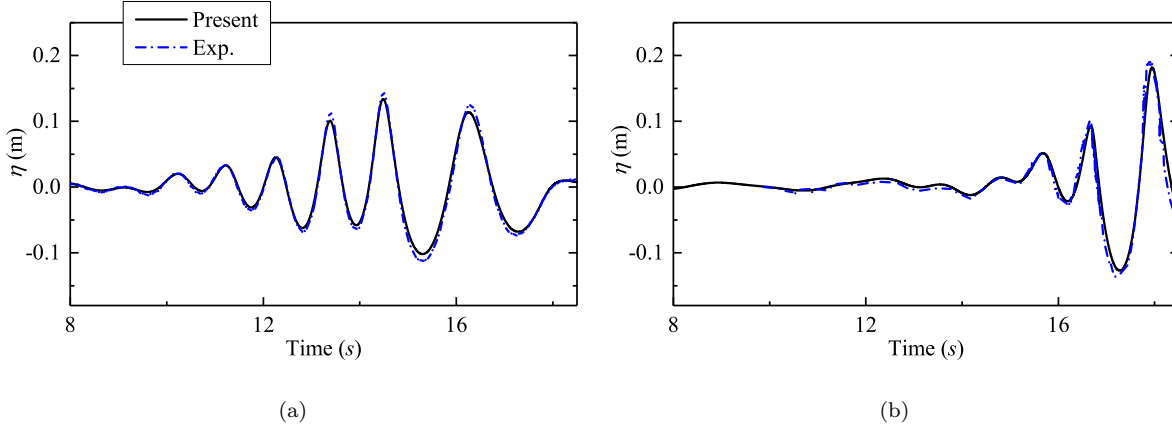


Figure 14: Comparison between the experimental and numerical wave elevations with for signal S2: (a) WG1; (b) WG3.

306 large cavity surrounding the front wall, resulting in the largest pressure value. The wave of S2 impacts the
 307 front wall slightly later than that at S1 but the pressure distribution along the front wall is slightly different
 308 compared with Fig. 16(a). Fig. 16(b) captures a high peak value of 9.01 kpa, close to the instant $t = 18.66$
 309 s Fig. 4. The Shape of Fig.16(b) is more like a pinnacle with a broader band than that in Fig. 16(a). In S3,
 310 the wave is not breaking yet when impacting on the platform (close to the instant $t = 18.70$ s Fig. 4), which
 311 leads to a distinguished wave impact pressure pattern, as shown in Fig.16(c). It is no longer an impulse in
 312 Fig. 16(a) or a pinnacle in Fig. 16(b). The maximal pressure value is located at $t = 18.7$ s, $y = 0.859$ m.
 313 As the bottom end of the front wall is still subjected to the propagating wave impact, the pressure value
 314 remains about 2.0 kpa at $y = 0.75$ m in Fig. 16(b) and Fig. 16(c).

315 The pressure distributions along the bottom wall under the three wave scenarios are presented in Fig. 17.
 316 For all 9 subfigures, with the distance far from the front wall (the upstream end of the bottom wall), the
 317 pressure begins to increase, reaching a maximum at a certain position, and reduces sharply to zero. The
 318 reason is that the whole bottom of the deck is not fully soaked. The part of the bottom wall contacting water
 319 is subjected to the larger pressure impact while the part contacting air bears very small pressure (almost
 320 zero). The pressure approaches the maximum at the demarcation point between the water and air on the
 321 bottom wall. The maximal pressure (3.47 kpa) on the bottom wall of S1 occurs at $t = 18.7$ s, $x = 13.80$
 322 m in Fig. 17(b). For the S2 wave scenario, the maximal pressure value (approximately 3.38 kpa) occurs in
 323 Fig. 17(d) at one end rather than in the middle of the bottom wall. As the corner connected to the front
 324 and bottom wall is still subjected to the wave impact in S2, a very high pressure is captured in the upstream
 325 end of bottom wall. But in Fig. 17(d), a peak pressure is captured at $t = 18.7$ s with the magnitude of 3.17
 326 kpa. In S3, The maximal pressure 3.16 kpa occurs at $t = 18.75$ s, $x = 14.12$ m. Those maximal pressures
 327 will be discussed in Fig. 18.

328 The spatial and temporal distribution of peak pressures on the front and bottom walls of the three cases

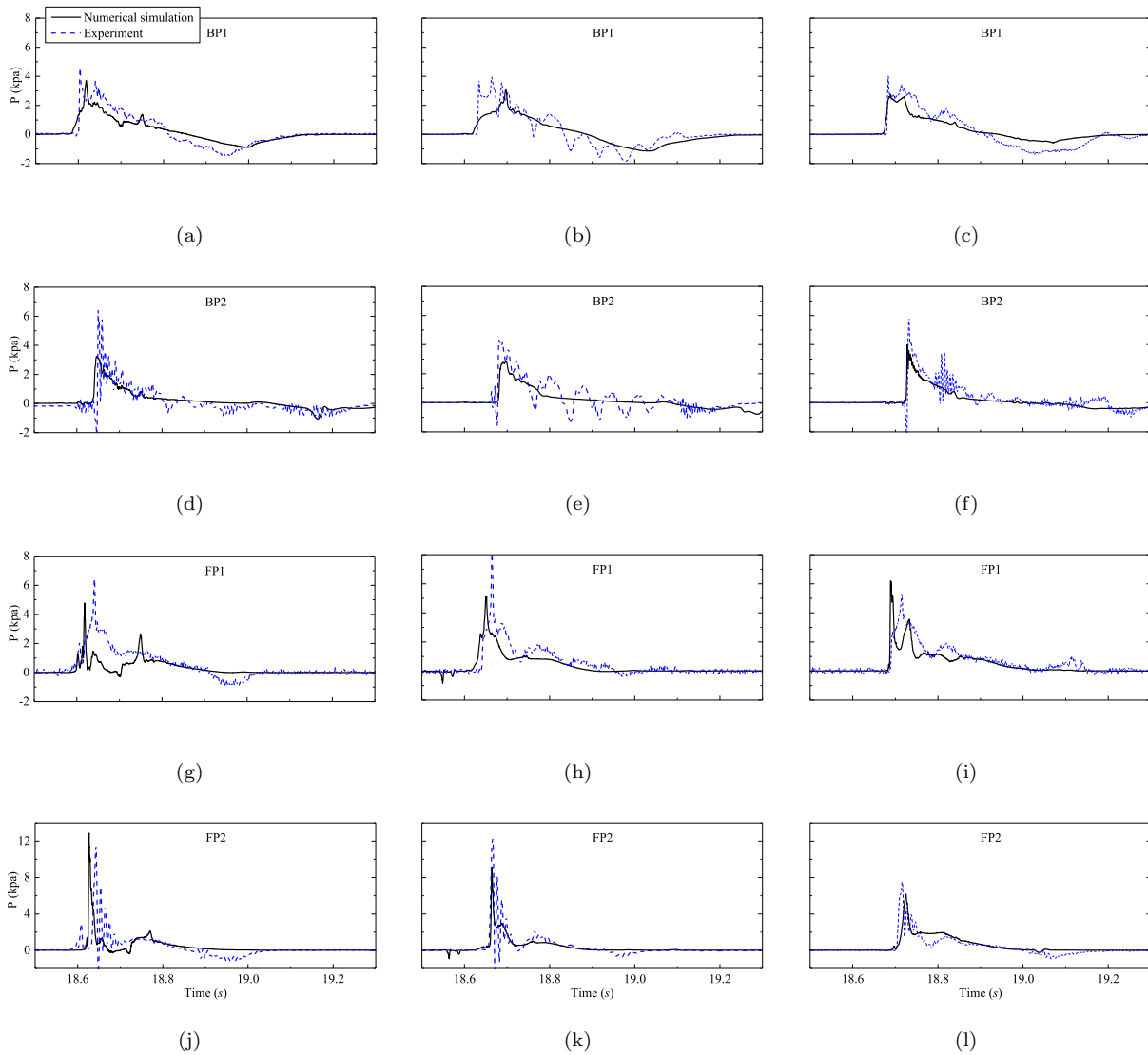


Figure 15: Comparison of impact pressures on the front (FP1 & FP2) and bottom (BP1 & BP2) walls of the platform for the 3 wave scenarios (left: S1; middle: S2; right: S3).

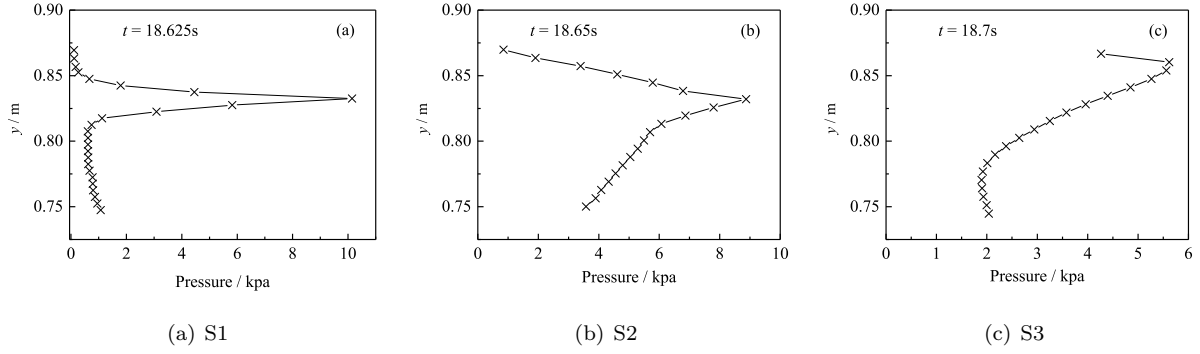


Figure 16: Pressure distributions along vertical front wall under the three wave scenarios: (a) S1. (b) S2; (c) S3.

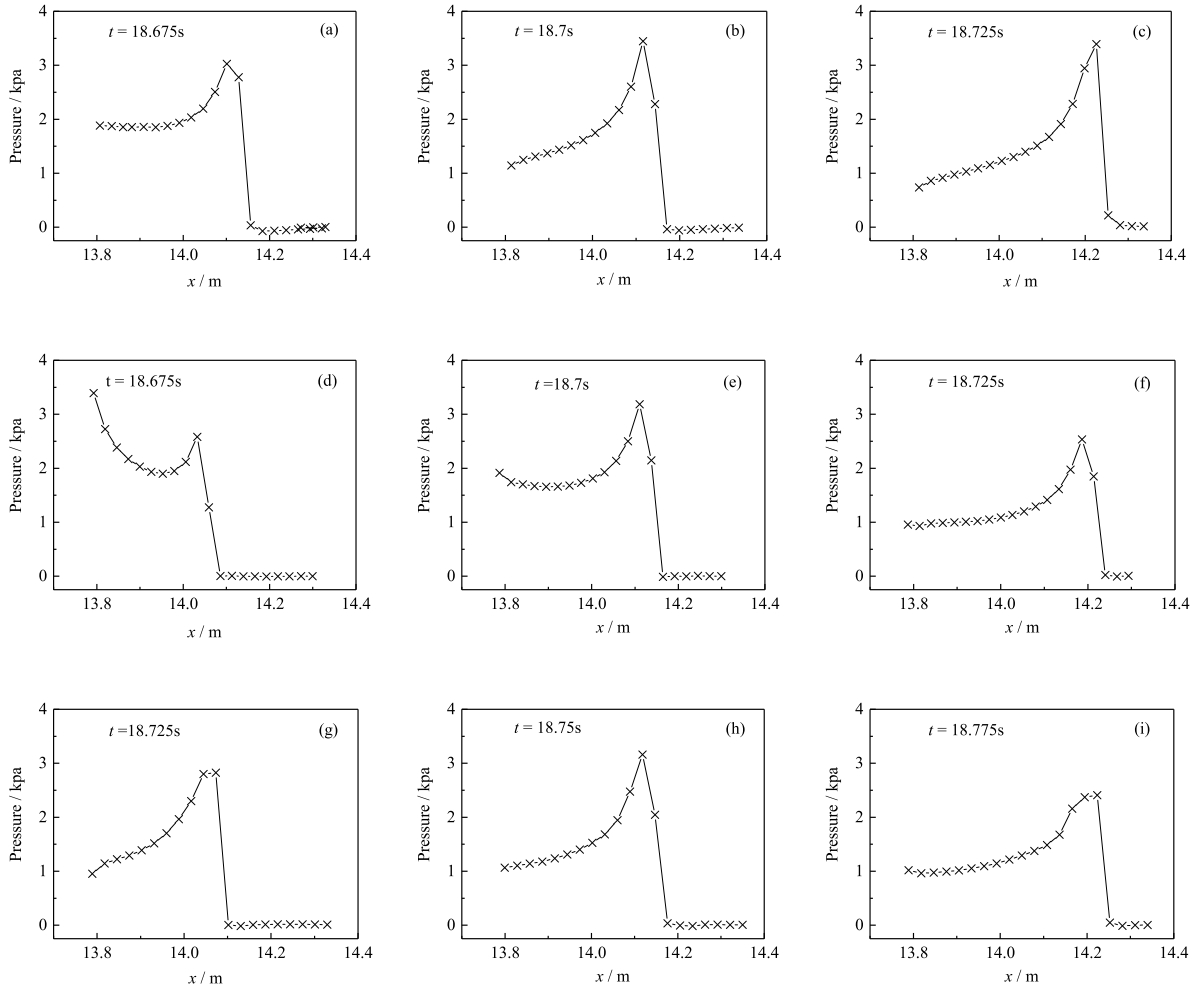


Figure 17: Pressure distributions along the horizontal bottom wall. Up row: S1; middle row: S2; bottom row: S3.

329 are presented in Fig. 18. In Fig. 18(a), the time interval of maximal pressure between S2 and S3 is almost
 330 two times of that between S1 and S2. The peak pressure bearing point moves upwards along the front wall
 331 from S1 to S3. Fig. 18(b) collects the maximal pressure points along the bottom wall. The maximal values
 332 for S1 and S2 occur at the very close position ($x = 14.12$ m). However, for S2, a special case happens that
 333 the maximal value occurs at one end of the bottom wall, rather than at the position around $x = 14.11$ m.
 334 At $x = 14.11$ m, S2 can still capture a peak value of 3.17 kpa, smaller than 3.38 kpa. The overall sequence
 335 of maximal pressure is $S1 > S2 > S3$.

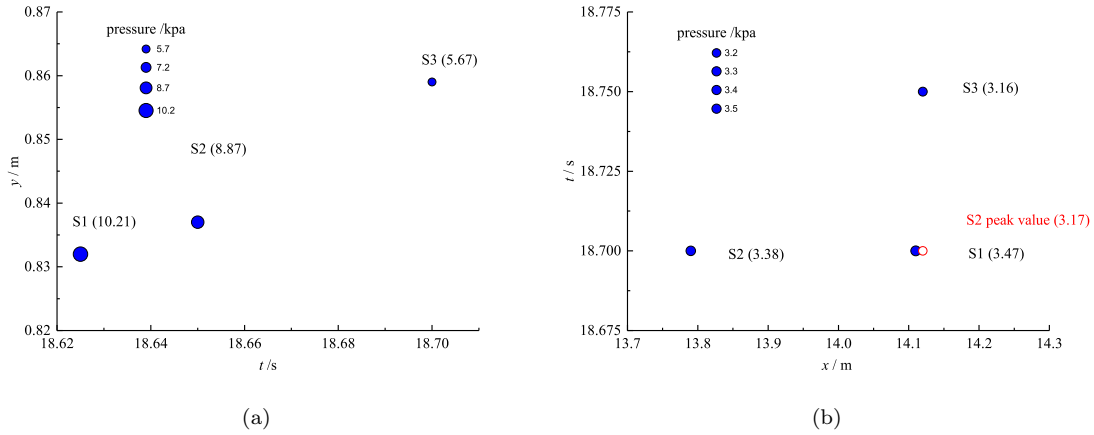


Figure 18: Spatial and temporal distribution of maximal pressure: (a) along the front wall; (b) along the bottom wall.

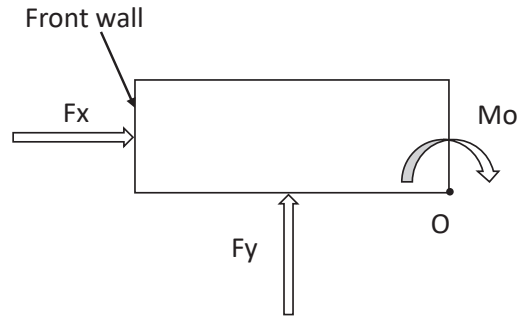
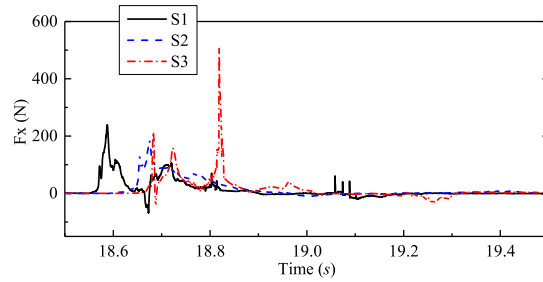


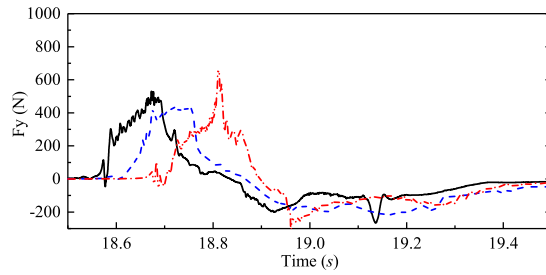
Figure 19: Sketch of force and moment directions on the platform.

336 In addition, the horizontal and vertical forces and moment (calculated on the rear of platform deck)
 337 on the platform are evaluated by integrating the wave impact pressure on the whole platform, which are
 338 presented in Fig. 20. To be clearly, the directions of force and moment on the platform are indicated in
 339 Fig. 19. These three sub-figures show the similar feature to the time histories of impact pressure. The time
 340 intervals of peak value among different wave impacts are the same indicated in Fig. 5. The only difference is
 341 that the wave impact S3 imposes the largest force and moment on the deck, as the area subjected to impact

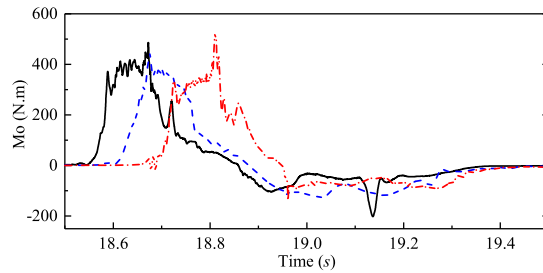
342 is larger. As the wave of S2 leads to the smaller impact pressure, an integration of impact pressure over the
 343 whole contact area is a little bit smaller. It is also observed that the loads of S3 are larger than those of S1
 344 and S2 (entrained more air). The magnitude of the force or moment is $S3 > S1 > S2$.



(a) Horizontal force



(b) Vertical force



(c) Moment

Figure 20: Horizontal, vertical force, and moment on the deck.

345 *3.5. Pressure maximum*

346 For the purpose of practical application, it is important to analyze the wave impact pressure or force as a
 347 dimensionless parameter. Two significant studies are Blackmore and Hewson (1984) and Cuomo et al. (2010).
 348 The peak pressures on the front wall of the box-shape structure in the present study are normalized by the
 349 approaches in these two studies, and compared with the documented peak pressure ranges, as presented in
 350 Table 4. The normalized pressure of S1 and S2 is larger than that of S1. And the wave scenarios S1 and S2
 351 entrain the air while there is little air entrapped in S3. It reveals that the air presence enlarges the impact

Table 4: Normalized pressure maximum on the front wall for different normalization approaches.

Types	$p_{max}/\rho C^2 T$			$p_{max}/\rho g H_D$	
	Present	Chan (1994)	Blackmore and Hewson (1984)	Present	Cuomo et al. (2010)
S1	1.86			3.89	
S2	1.77	8.8~18.5	1~10	3.70	1.0~4.5
S3	1.06			2.22	

352 pressure, consistent with the conclusions in Wood Deborah et al. (2000) and Bredmose et al. (2015). It
 353 also finds that the maximal pressures on a fixed box structure under the plunging wave circumstances of
 354 this study are located in the observed pressure ranges by Blackmore and Hewson (1984) and Cuomo et al.
 355 (2010). The normalized pressure from Chan (1994) deviates much from the range 1~10. It also reflects the
 356 bad repeatability of experiments, stated in Subsection 2.4. Conducting more work so as to figure out a more
 357 accurate peak pressure range for the box-shape structure is of great significance, which will be the future
 358 work.

359 4. Conclusions

360 The paper investigates the plunging wave impacts on a box-shape structure experimentally and numeri-
 361 cally. Three impact scenarios are studied, i.e. impact after wave breaking (S1), impact upon wave breaking
 362 (S2), and impact before wave breaking (S3). Both experimental and numerical results show that the impacts
 363 of S1 and S2 possess the similar pressure magnitudes. The front wall bears the larger impact pressure than
 364 the bottom wall. The pressure oscillation is observed on the front wall that it is strongly correlated with
 365 the evolution of air cavity by examining the area of air cavity. The existence of air cavity results in the
 366 larger maximal positive and negative pressure. The amplified pressure easily causes the local damages to the
 367 designed structure. In addition, the repeatability test of S2 are carried out for three times that the pressure
 368 time histories repeat well. The numerical results from an improved immersed boundary method is compared
 369 with the experiment. A roughly good agreement is obtained for the wave elevations. The numerical method
 370 captures the key features of impact pressures. The numerical pressure distributions reflect that the pressure
 371 distributions on the front wall under three wave scenarios follow different modes. However, it is very similar
 372 for the pressure distributions on the bottom wall under the three wave scenarios.

373 Finally, two normalizations for pressure maximum are presented that the present normalized pressure
 374 maximums are located in the corresponding range of Blackmore and Hewson (1984) and Cuomo et al. (2010).
 375 However, the normalized pressure maximum from Chan (1994) is much larger than the present result. It
 376 also deviates much from the range of 1 ~ 10. By the comparison of the maximal impact pressures among
 377 three wave scenarios, the presence of aeration indeed increases the impact pressure maximum.

378 **References**

- 379 Abdussamie, N., Ojeda, R., Thomas, G. and Amin, W. (2016). Measurements of global and local effects of
380 wave impact on a fixed platform deck, *Proceedings of the Institution of Mechanical Engineers, Part M:
381 Journal of Engineering for the Maritime Environment* **231**(1): 212–233.
- 382 Abrahamsen, B. C. and Faltinsen, O. M. (2012). The natural frequency of the pressure oscillations inside a
383 water-wave entrapped air pocket on a rigid wall, *Journal of Fluids and Structures* **35**: 200–212.
- 384 Archer, P. and Bai, W. (2015). A new non-overlapping concept to improve the hybrid particle level set
385 method in multi-phase fluid flows, *Journal of Computational Physics* **282**: 317–333.
- 386 Biesel, F. and Suquet, F. (1951). Les appareils generateurs de houle en laboratoire, *La Houille Blanche* **6**: 4.
- 387 Blackmore, P. A. and Hewson, P. J. (1984). Experiments on full-scale wave impact pressures, *Coastal
388 Engineering* **8**(4): 331–346.
- 389 Bredmose, H., Bullock, G. N. and Hogg, A. J. (2015). Violent breaking wave impacts. Part 3. effects of scale
390 and aeration, *Journal of Fluid Mechanics* **765**: 82–113.
- 391 Bredmose, H., Hunt Raby, A., Jayaratne, R. and Bullock, G. N. (2010). The ideal flip-through impact:
392 experimental and numerical investigation, *Journal of Engineering Mathematics* **67**(1): 115–136.
- 393 Bullock, G. N., Obhrai, C., Peregrine, D. H. and Bredmose, H. (2007). Violent breaking wave impacts.
394 Part 1: Results from large-scale regular wave tests on vertical and sloping walls, *Coastal Engineering*
395 **54**(8): 602–617.
- 396 Chan, E. S. (1994). Mechanics of deep water plunging-wave impacts on vertical structures, *Coastal Engi-
397 neering* **22**(1): 115–133.
- 398 Chan, E. S. and Melville, W. K. (1988). Deep-water plunging wave pressures on a vertical plane wall,
399 *Proceedings of the Royal Society of London A: Mathematical, Physical and Engineering Sciences*, Vol. 417,
400 pp. 95–131.
- 401 Cuomo, G., Allsop, W., Bruce, T. and Pearson, J. (2010). Breaking wave loads at vertical seawalls and
402 breakwaters, *Coastal Engineering* **57**(4): 424–439.
- 403 Faltinsen, O. M., Landrini, M. and Greco, M. (2004). Slamming in marine applications, *Journal of Engi-
404 neering Mathematics* **48**(3): 187–217.
- 405 Gao, R., Ren, B., Wang, G. and Wang, Y. (2012). Numerical modelling of regular wave slamming on subface
406 of open-piled structures with the corrected sph method, *Applied Ocean Research* **34**: 173–186.

- 407 Guilcher, P.-M., Couty, N., Brosset, L. and Le Touz, D. (2013). Simulations of breaking wave impacts on a
408 rigid wall at two different scales with a two-phase fluid compressible sph model, *International Journal of*
409 *Offshore and Polar Engineering* **23**(4): 182–190.
- 410 Hu, Z. Z., Mai, T., Greaves, D. and Raby, A. (2017). Investigations of offshore breaking wave impacts on a
411 large offshore structure, *Journal of Fluids and Structures* **75**: 99–116.
- 412 Jiang, G. and Peng, D. (2000). Weighted ENO schemes for Hamilton-Jacobi equations, *SIAM Journal on*
413 *Scientific Computing* **21**(6): 2126– 2143.
- 414 Lind, S. J., Stansby, P. K., Rogers, B. D. and Lloyd, P. M. (2015). Numerical predictions of waterair
415 wave slam using incompressiblecompressible smoothed particle hydrodynamics, *Applied Ocean Research*
416 **49**: 57–71.
- 417 Lugni, C., Brocchini, M. and Faltinsen, O. M. (2010). Evolution of the air cavity during a depressurized
418 wave impact. ii. the dynamic field, *Physics of Fluids* **22**(5): 056102.
- 419 Luo, M., Koh, C. G., Bai, W. and Gao, M. (2016). A particle method for two-phase flows with compressible
420 air pocket, *International Journal for Numerical Methods in Engineering* **108**(7): 695–721.
- 421 Ma, Y., Dong, G., Perlin, M., Liu, S., Zang, J. and Sun, Y. (2009). Higher-harmonic focused-wave forces on
422 a vertical cylinder, *Ocean Engineering* **36**(8): 595–604.
- 423 Mohd-Yusof, J. (1997). Combined immersed boundary/B-spline method for simulations of flows in complex
424 geometries, *Technical report*, Center Annual Research Briefs, NASA Ames/Stanford University.
- 425 Qin, H., Tang, W., Xue, H. and Hu, Z. (2017). Numerical study of nonlinear freak wave impact underneath
426 a fixed horizontal deck in 2-d space, *Applied Ocean Research* **64**: 155–168.
- 427 Ren, B., Li, X. L. and Wang, Y. X. (2006). Experimental investigation of instantaneous properties of the
428 flow field of wave slamming, *Ocean Engineering* **24**(4): 68–74.
- 429 Topliss, M., Cooker, M. and Peregrine, D. (1993). Pressure oscillations during wave impact on vertical walls,
430 *23rd International Conference on Coastal Engineering*.
- 431 Wood Deborah, J., Peregrine, D. H. and Bruce, T. (2000). Wave impact on a wall using pressure-impulse
432 theory. Part I: Trapped air, *Journal of Waterway, Port, Coastal, and Ocean Engineering* **126**(4): 182–190.
- 433 Yan, B., Bai, W. and Quek, S. T. (2018). An improved immersed boundary method with new forcing point
434 searching scheme for simulation of bodies in free surface flows, *Communications in Computational Physics*
435 **24**(3): 830–859.
- 436 Zhao, X. and Hu, C. (2012). Numerical and experimental study on a 2-D floating body under extreme wave
437 conditions, *Applied Ocean Research* **35**: 1–13.